

FIRST EVIDENCE OF A PRECESSING JET EXCAVATING A
PROTOSTELLAR ENVELOPE

A thesis submitted to the faculty of
San Francisco State University
In partial fulfillment of
The requirements for
The degree

Master of Science
In
Physics

by

Jason E. Ybarra

San Francisco, California

August, 2006

CERTIFICATION OF APPROVAL

I certify that I have read *First Evidence of a Pre-processing Jet Excavating a Protostellar Envelope* by Jason E. Ybarra, and that in my opinion this work meets the criteria for approving a thesis submitted in partial fulfillment of the requirements for the degree: Master of Science in Physics at San Francisco State University

Adrienne M. Cool
Professor of Physics

Ronald O. Marzke
Professor of Physics

Mary Barsony
Professor of Physics

FIRST EVIDENCE OF A PRECESSING JET EXCAVATING A
PROTOSTELLAR ENVELOPE

Jason E. Ybarra
San Francisco State University
2006

To explore the relationship between the infall envelope and the outflow, narrowband H_2 1–0 S(1), $\text{Br}\gamma$, and K_{cont} filters were used to image the Class I protostar, Elias 29, with the Wide-Field Infrared Camera on the Hale 5.0-meter telescope and with Persson's Auxiliary Nasmyth Infrared Camera on the Baade 6.5-meter telescope. The source appears as a bipolar, scattered light nebula, with a wide opening angle as is typical for late-stage protostars. However, the pure H_2 emission-line images point to the presence of a heretofore undetected precessing jet. It is argued that high velocity, narrow, precessing jets provide the mechanism for creating the observed wide-angled outflow cavity in this source.

I certify that the Abstract is a correct representation of the content of this thesis.

Chair, Thesis Committee

Date

ACKNOWLEDGMENTS

I would like to thank and express my appreciation to my advisor, Mary Barsony, for her invaluable guidance and advice. I thank Karl Haisch and Tom Jarrett for advice with the data reduction and also Alycia Weinberger and Raghvendra Sahai for their valuable suggestions. I also thank my thesis committee for their suggestions and guidance.

I would like to thank my undergraduate advisor, Randy Phelps for his continued advice and for introducing me to the study of star formation. I also would like to thank Harriet Taniguchi who encouraged me seek out research opportunities. I would like to thank my friends, Raman Narayan and Bret van den Akker, for keeping me sane during these last two years. I would like to thank my parents Arleen and Winfried Bauer for their love and encouraging me to achieve my goals. I would like to thank everyone who directly or indirectly helped me finish this thesis. My deepest gratitude goes to my wife, River Ybarra, for her love and support. Her patience and understanding made it possible for me to finish this thesis.

TABLE OF CONTENTS

List of Tables	vi
List of Figures	vii
1 Introduction	1
1.1 Molecular outflows and Jets	1
1.2 Jet Precession	3
1.3 Wide-angle wind vs. precessing jet geometries	4
1.4 Molecular hydrogen as a tracer of jet activity	4
2 Observations	7
2.1 Palomar Observatory	7
2.2 Las Campanas Observatory	8
3 Data Reduction	10
3.1 Reduction of Palomar WIRC data	10
3.2 Reduction of Magellan PANIC data	10
3.3 Continuum Subtraction	11
3.4 Astrometry	14
4 Results	15
5 Discussion	20
5.1 Comparison to hydrodynamic simulations	21
5.2 Comparison to observations of other Young Stellar Objects . .	23
5.3 Precession Mechanisms	24
5.4 Conclusion	25
References	27
A IRAF grid.cl script	31

LIST OF TABLES

Table		Page
1	Comparison of optical jets to outflows	1
2	H ₂ emission features	17

LIST OF FIGURES

Figure		Page
1	Wide-angled wind vs. jet-driven wind model geometries	4
2	SED of Elias 29	12
3	PANIC filter profiles	13
4	Comparison of WIRC and PANIC images of Elias 29	18
5	PANIC Br γ and pure H ₂ emission line images of Elias 29 . . .	19
6	Jet simulation images	22
7	Comparison of simulations to H ₂ emission from Elias 29	23

1 Introduction

Parts of this thesis comprise a paper by J. E. Ybarra, M. Barsony, K. E. Haisch, T. H. Jarett, R. Sahai, & A. J. Weinberger. Accepted for publication in The Astrophysical Journal Letters

1.1 Molecular outflows and Jets

Powerful, bipolar outflows are a hallmark of the earliest stages of star formation. Such flows carry away excess angular momentum thus allowing the protostar to continue accreting material and preventing it from breakup. Outflows were first discovered in millimeter observations of the CO molecule (Zuckerman et al. 1976; Snell et al. 1980). These molecular outflows generally exhibit wide opening angles and have typical velocities of $\sim 10\text{-}30 \text{ km s}^{-1}$. Narrow, highly collimated optical jets powered by protostars were discovered with the advent of narrowband CCD imaging (Mundt & Fried 1983). These jets exhibit small opening angles and velocities of $\sim 100\text{-}400 \text{ km s}^{-1}$ (Mundt et al. 1990; Königl & Pudritz 2000).

Table 1: Comparison of optical jets to outflows

	Optical Jets	Molecular Outflows
Velocities	100-400 km s^{-1}	10-30 km s^{-1}
Opening angle	$< 10^\circ$	$\sim 90^\circ$

Different views have arisen about the origin of the molecular outflows and

optical jets. On account of the disparate spatial and velocity distribution between the molecular flows and optical jets, a two-wind structure has been suggested to explain the simultaneous occurrence of both outflow components (Stocke et al. 1988; Davis et al. 2002; Liseau et al. 2005). In this view a wide-angle wind has a density distribution that is enhanced along the axis exhibiting a collimated jet-like appearance (Reipurth & Bally 2001; Shu et al. 1995). However, in an alternate scenario, optical jet and molecular outflows result from a single, collimated flow (Hartigan et al. 1994; Sandell et al. 1999; Wolf-Chase et al. 2000; Yun et al. 2001). Initially, there appeared to be a discrepancy between the momentum supply rate inferred from observations of optical jets to that required to power the larger scale molecular outflows. However, ionization fractions based on line ratio analysis of optical jets were found to be lower than originally thought and accordingly the jet mass-loss rates are higher than the earlier estimates (Hartigan et al. 1994). Additionally, the total age of jets and outflows was recognized to be $\sim 2 \times 10^5$ yr, an order of magnitude longer than their inferred dynamical times (Parker et al. 1991). Thus, the momentum supplied by the jets is consistent with that of the molecular outflows.

1.2 Jet Precession

An outstanding, unsolved problem with jet-driven outflow models is how jets produce the wide-angle outflow cavities observed in both protostellar envelopes and in molecular outflows. A proposed solution is that of jets changing direction (Masson & Chernin 1993), for which there is now growing evidence (Bence et al. 1996; Reipurth et al. 1997; Barsony et al. 1998; Arce & Sargent 2005). Nevertheless, the spatial relationship between the outflow cavity and the currently active wandering jet has not yet been directly observed within the boundaries of a protostellar envelope. Optical manifestations of protostellar jets are not observable within their dense infall envelopes, and the cold molecular gas amenable to observation with millimeter/submillimeter interferometry cannot trace the variation of the jet's location on precession timescales. However, infrared H₂ imaging can penetrate regions that optical imaging cannot, and because of its short cooling time, can explore jet variations on rapid timescales. Thus in order to study the relationship between the jet and outflow cavity narrowband near-infrared H₂ imaging must be used.

1.3 Wide-angle wind vs. precessing jet geometries

The wind-angle wind and precessing jet-driven models predict different geometries. Thus it is possible to observationally distinguish the models. Due to the density distribution in the wide-angle wind model, the jet manifests itself along the flow axis. For the precessing jet model, the jet is not constrained to the outflow axis but is free to move about the cavity and also interact with the cavity walls. Given the bipolar nature of the jets, the jets exhibit an S -shaped point symmetry about the source (fig 1). Consequently observations can reveal the nature of the jet and outflow.

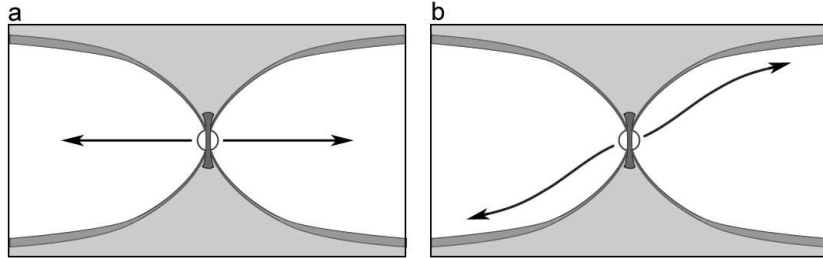


Figure 1: Geometries of the jet, cavity, and outflow for the (a) Wide-angle wind model and (b) Precessing jet-driven wind model. Jet location is indicated with the black lines with arrows

1.4 Molecular hydrogen as a tracer of jet activity

Molecular hydrogen is the main near-infrared coolant of shocked gas in outflows. The brightest H_2 line is from the $2.122 \mu\text{m}$ 1-0 S(1) quadrupole transi-

tion. The H₂ molecule is collisionally excited in shocked gas at temperatures of a few 1000 K (Reipurth & Bally 2001; Richer et al. 2000). Proper motion studies show NIR H₂ emission in jets typically moving at high velocities of hundreds of kilometers per second similar to the velocities of their optical Herbig-Haro counterparts (Eisloffel et al. 2000; Reipurth & Bally 2001). Since the shock speed for molecular dissociation is an order of magnitude less (Lepp & Shull 1983), the emission seen arises from molecular gas that is moving with the jet. The cooling time for the H₂ 1–0 S(1) transition can be estimated with the following formula

$$t_c = \frac{1.5kT_s}{f_j A_{ij} E_{ij} \gamma_{ij}}$$

where T_s is the post-shock temperature, f_j is the fraction of H₂ in the j th state, A_{ij} is the emission rate, E_{ij} is the transition energy, and γ_{ij} is the total emission over the line emission. The emission rate for the 1–0 S(1) transition is $3.48 \times 10^{-7} \text{ s}^{-1}$ and the ratio of total emission over the line emission is on average $\gamma = 13$ for shock velocities $\sim 10 \text{ km s}^{-1}$ (Hollenbach & Shull 1977; Shull & Hollenbach 1978). The energy of the transition can be gotten from $E = \frac{hc}{\lambda} = 9.4 \times 10^{-20} \text{ J}$. Assuming a post shock temperature of 3000 K and the fraction of H₂ in the $v = 1, J = 3$ state is 10^{-3} (Shull & Hollenbach 1978) we get a cooling time $t_c \sim 5 \text{ yr}$. Since the cooling times for H₂ emission

are on the order of years, H₂ emission traces the current location of the jet interaction with the environment (Eisloffel et al. 2000). Therefore, we use sensitive, narrowband near-infrared imaging to study the relationship between the jet and outflow cavity: the scattered light emission from the protostellar envelope is imaged with a narrowband continuum filter, whereas the currently active jet regions within the infall envelope are traced in continuum-subtracted, narrowband H₂ images, sensitive to shock-excited emission. Based on such observations of the Class I protostar, Elias 29=WL15 ($\alpha_{2000} = 16^h27^m09.43^s$, $\delta_{2000} = -24^\circ37'18''.7$) in the nearby (d = 125 pc) ρ Ophiuchi molecular cloud, we report the first detection of a precessing jet carving out a protostellar envelope's cavity.

2 Observations

2.1 Palomar Observatory

Near-infrared, narrowband imaging of Elias 29 was undertaken at Palomar Observatory using the Wide Field Infrared Camera (WIRC) on the Hale 5.0-meter telescope. WIRC, with its $8'.7 \times 8'.7$ field of view, was used to image the field including Elias 29 (Wilson et al. 2003). WIRC employs a 2048×2048 pixel Hawaii-II detector with a plate-scale of $0''.2487 \text{ pixel}^{-1}$. The K-band seeing was $\sim 1''.0$ on the night of the observations, 2004 July 11. Two narrowband filters were used for imaging: an H_2 1–0 S(1) filter centered at $2.120 \mu\text{m}$ with a 1.5% bandpass and a line-free continuum filter (K_{cont}) centered at $2.270 \mu\text{m}$ with a 1.7% bandpass.

The telescope was dithered in a nine-point pattern, with $6''$ offsets between dither positions. The integration time at each dither position was 60 sec (30 sec x 2 coadds). The dither pattern was repeated, after a $5''$ offset of the telescope, until a total integration time of 27 minutes was reached in each filter. Individual exposures of 30 seconds were chosen to reach the sky-background limited noise through each narrowband filter.

2.2 Las Campanas Observatory

Elias 29 was re-observed with Persson’s Auxiliary Nasmyth Infrared Camera (PANIC) on the Baade 6.5-meter telescope at Las Campanas Observatory (LCO) on the night of 2005 June 17 UT. The K-band seeing was $0''.5$. PANIC employs a 1024×1024 Hawaii-I detector with a plate scale of $0''.125 \text{ pixel}^{-1}$ (Martini et al. 2004). The two narrowband filters used for imaging at LCO were the H_2 1–0 S(1) filter centered at $2.125 \mu\text{m}$ with a 1.1% bandpass, and the $\text{Br}\gamma$ filter, centered at a wavelength of $2.165 \mu\text{m}$ with a 1.0% bandpass. In the absence of a specific narrowband continuum filter to complement the H_2 filter at PANIC, the available $\text{Br}\gamma$ filter served as the narrowband continuum filter instead. This substitution is justified for purposes of continuum subtraction to detect pure H_2 outflow emission, since low-velocity shocks that emit in the near-infrared H_2 lines are not sufficiently energetic to excite $\text{Br}\gamma$ emission (Hodapp 1999).

The observing pattern for Elias 29 at LCO consisted of interleaved on- and off-source integrations, of 30 sec duration each, through each filter. On-source integrations were dithered in a checkerboard pattern, with $12''$ offsets. Separate five-point dithered sky observations were taken in a clear patch $3''$ E of Elias 29. The final on-source integration times with PANIC were 70 mins.

through the H₂ filter and 67.5 mins. through the Br γ filter.

3 Data Reduction

3.1 Reduction of Palomar WIRC data

Data were reduced using IRAF¹. For each object frame a sky frame was created from the 9 dithered frames closest in time to the object frame. These dithered frames were median averaged to get rid of stellar components and background variations. Before averaging, the frames were scaled to the object frame by a median value computed from the image statistics thus compensating for the small time variations in the background level. The object frames were then sky subtracted, flat-fielded by dividing the object frame by the normalized sky frame (Appendix A). The object frames were then corrected for bad pixels and aligned with the IRAF task IMCENTROID using available point sources common to the individual frames. Processed frames for each filter were combined to produce the final images.

3.2 Reduction of Magellan PANIC data

PANIC data were first linearized with the custom IRAF task, *lincor*, and then corrected for instrumental radial distortion with the custom IRAF task,

¹IRAF is distributed by the National Optical Astronomy Observatories, which are operated by the Association of Universities for Research in Astronomy, Inc., under cooperative agreement with the National Science Foundation.

distcor. PANIC-specific IRAF tasks were obtained from the PANIC Data Reduction Package². Sky frames were constructed from median combining the 5 dithered, off-source, sky observations specially obtained for this purpose, nearest in time to the object frames. Flat fields were produced from normalizing the set of sky frames. The object frames were sky-subtracted, flat-fielded, corrected for bad pixels, and aligned. The final images were produced by combining the aligned object frames.

3.3 Continuum Subtraction

Although the H₂ filters are so-called because they transmit the 2.12 μm emission line, they also transmit some continuum emission, if present, in the source. Therefore to trace the morphology of any outflow/jet component within the protostellar envelope of Elias 29, the bright continuum emission from the scattering envelope must be subtracted from the H₂ filter images. This requires proper scaling and alignment of the narrowband “continuum” images before subtracting them from the respective H₂ filter images.

For the WIRC data, the ratio of the transmission of the H₂ filter to that of the narrowband continuum filter (K_{cont}) is 0.93 from the filter transmission

²P. Martini and E. Persson, PANIC Data Reduction Package 0.95 (Carnegie Observatories)

curves. This ratio can be calculated as follows:

$$\text{transmission ratio} = \frac{\int S_{f_1}(\lambda)d\lambda}{\int S_{f_2}(\lambda)d\lambda}$$

where S_{f_1} is the transmission of the H₂ filter and S_{f_2} is the transmission of the K_{cont} filter. A further scaling factor of 0.6 was applied to the K_{cont} image to account for the steepness of the spectral energy distribution (SED) of Elias 29 between 2.12 μm and 2.27 μm (Greene & Lada 1996). This additional scaling factor is the ratio of flux at 2.12 μm to that at 2.27 μm as estimated from the SED (see fig 2). For the PANIC images, the Br γ filter image was scaled

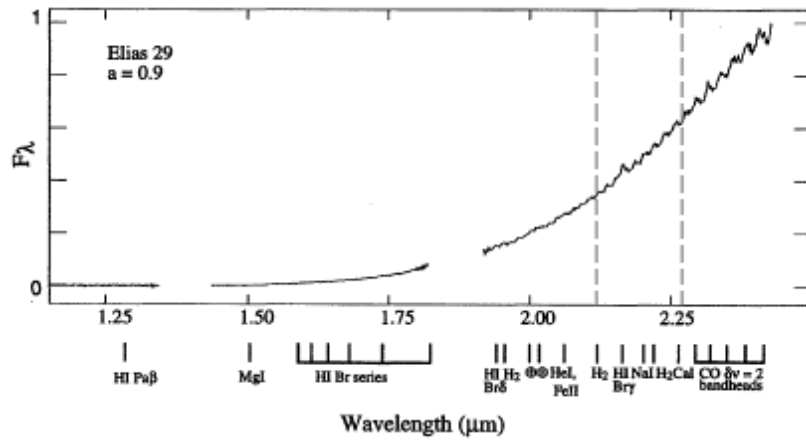


Figure 2: Spectral energy distribution (SED) of Elias 29 from Greene & Lada (1996). The positions of 2.12 μm and 2.27 μm are indicated with broken lines.

by 0.82, which is simply the ratio of the transmission of the H₂ filter to that of the Br γ filter, from the filter transmission curves (Figure 3). The central

wavelengths of the H₂ (2.125 μm) and Br γ (2.165 μm) filters are close enough that the continuum emission from Elias 29 is essentially constant, thus no further scaling factor correction was needed. Proper alignment of the H₂ and scaled “continuum” images before subtraction, which is crucial for obtaining accurate pure H₂ line-emission images, was achieved by using the IRAF task, IMCENTROID, for point sources in common to the final images in each filter

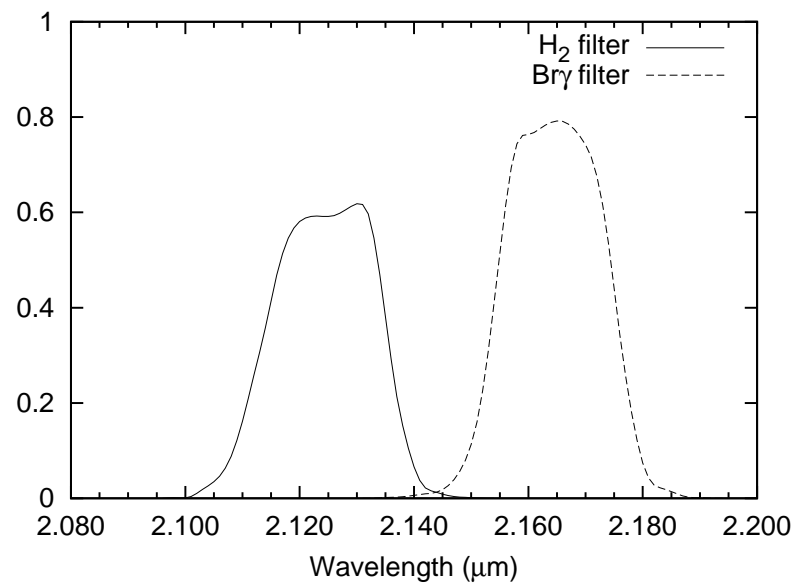


Figure 3: PANIC H₂ and Br γ filter profiles (E. Persson, prov. comm. 2005)

3.4 Astrometry

For astrometry, a plate solution was determined for the WIRC data by using a least squares fit for 7 point objects in common with 2MASS³. The 2MASS reference objects had uncertainty ellipses of $\sim 0''.09$ (Skrutskie et al. 2006). The plate solution had a $0''.2$ RMS residual, our estimated astrometric uncertainty.

³<http://www.phys.vt.edu/~jhs/SIPbeta/astrometrycalc.html>

4 Results

Figure 4 shows the reduced images of Elias 29 from WIRC in the top panels and from PANIC in the bottom panels. The reduced WIRC and PANIC images of Elias 29 appear essentially identical, however the PANIC images were obtained in better seeing and have higher signal-to-noise. The images are presented in a linear greyscale stretch to emphasize the presence of the pure emission features, 3a and 3b in Figures 4a and 4d, and their absence from Figures 4b and 4e. Figures 4a and 4d show the appearance of Elias 29 through the WIRC and PANIC narrowband H₂ filters respectively. Figure 4b shows Elias 29 through the WIRC narrowband K_{cont} filter and Figure 4e shows Elias 29 through the surrogate “narrowband continuum” (Br γ) filter. Since the NIR continuum emission overwhelms the strength of the pure H₂ line emission for this object, Elias 29 looks similar in the H₂ and respective narrowband continuum images. Figures 2c and 2f show the continuum-subtracted, pure H₂ emission-line image of Elias 29. Saturation effects from the extreme brightness of Elias 29 prevent correct image subtraction within the central $\sim 5''.5$ radius region, resulting in artifacts at the center of the figure. Outside this area, five regions of pure H₂ line emission are discovered, having been missed by previous investigators (Gómez et al. 2003; Khanzadyan et al. 2004).

The appearance of Elias 29 in the H₂ and continuum images is consistent with scattered light models of Class I protostars consisting of an infall envelope containing a bipolar cavity (Whitney et al. 2003). The boundary of the wide-angled cavity walls within the protostellar infall envelope is indicated by the 10- σ contour overplotted on Figures 3a & 3b. The lack of a narrow “waist” or distinctive hourglass shape at this angular resolution is consistent with the presence of a disk of small spatial extent (B. Whitney, priv. comm.). The pure H₂ emission objects, labeled 1, 2a, 2b, 3a, and 3b, appear at the same location, and have similar morphologies in both the PANIC and the WIRC continuum-subtracted H₂ images. Taken together, the H₂ emission knots form a sinuous structure with S-shaped point-symmetry about the center.

Table 1 lists the observed characteristics of each H₂ feature. The first column lists the feature designations from Figure 1c. The second and third columns list the coordinates of each H₂ emission region, corresponding to the location of the brightest emission within each object. The coordinates are derived from the WIRC data, since there were not enough sources in the smaller PANIC field to provide a plate solution for absolute astrometry. The final, continuum-subtracted PANIC image was used to determine the signal to noise ratio of each emission feature, listed in the last column of Table 1, since

the seeing and signal to noise were better in the PANIC than in the WIRC dataset. A rectangular aperture (of dimensions given in the fourth column of Table 1) was used to determine the average counts in each feature. Several background regions were used to calculate the average background noise level and its standard deviation. The background level was subtracted from the average counts in the rectangular aperture containing each H₂ emission region, and the result was divided by the standard deviation of the background to give the SNR. Only features 3a and 3b have $\sigma < 3$. Nevertheless, these objects are real, since they appear at identical locations and have similar morphologies in both datasets (WIRC and PANIC).

Table 2: H₂ emission features

H ₂ Feature Designation	α_{2000} (h m s)	δ_{2000} ° ' "	Aperture	S/N
1	16 27 08.79	-24 37 16.5	0'6 × 0'5	3.5
2a	16 27 10.04	-24 37 20.8	0'6 × 0'5	3.9
2b	16 27 10.70	-24 37 24.3	1'3 × 0'5	14.2
3a	16 27 11.64	-24 37 56.1	0'6 × 0'5	2.6
3b	16 27 11.88	-24 38 00.0	0'9 × 0'4	2.8

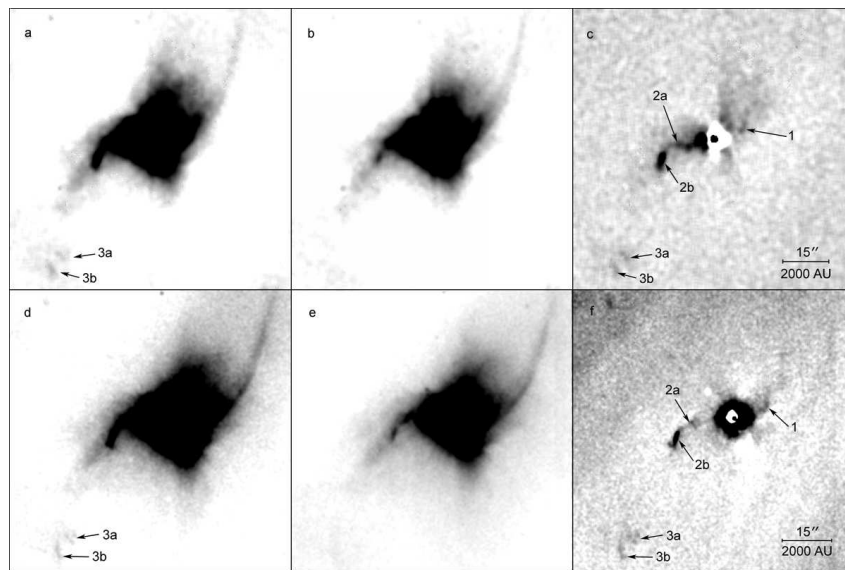


Figure 4: Narrowband Images of Elias 29. N is up and E is left in all panels. (a) WIRC narrowband H_2 filter (b) WIRC narrowband continuum filter, K_{cont} (c) Pure H_2 emission line image of Elias 29, obtained by subtracting the scaled and aligned K_{cont} image from the H_2 filter image (d) PANIC narrowband H_2 filter (e) PANIC narrowband $Br\gamma$ filter (f) Pure H_2 emission line image of Elias 29, obtained by subtracting the scaled and aligned $Br\gamma$ image from the PANIC H_2 filter image

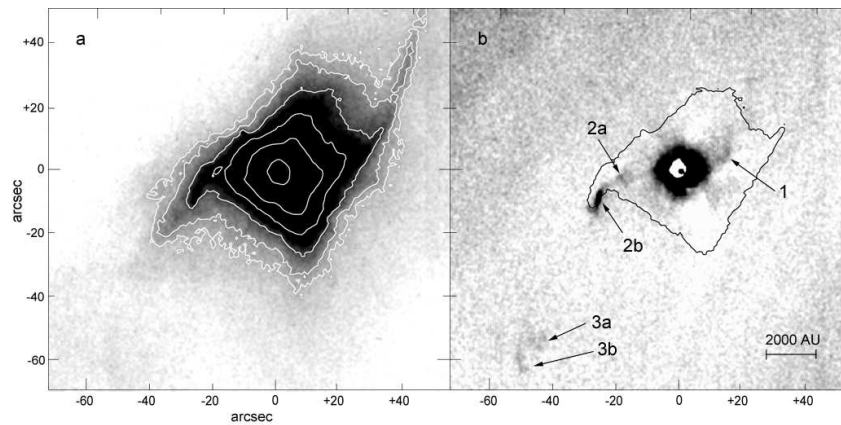


Figure 5: Narrowband Images of Elias 29. N is up and E is left in all panels. Offsets from RA(2000)= $16^h27^m09.43^s$ and Dec(2000)= $-24^\circ37'18''.7$ are indicated, in arcsec units. (a) Elias 29 imaged with the Br γ filter with PANIC, contour levels are 3, 5, 10, 20, 50, 500 σ . Note the absence of Features 3a and 3b in the Br γ image, and their presence in the H $_2$ filter image. (b) Pure H $_2$ emission-line image of Elias 29, obtained by subtracting the scaled and aligned Br γ filter image from the PANIC H $_2$ filter image with the Br γ 10- σ contour superimposed. The pure H $_2$ emission line features discussed in the text and listed in Table 1 are labeled.

5 Discussion

H₂ emission associated with molecular outflows generally arises from shock interactions of the unseen, fast jet/wind component with the ambient medium. Elias 29 is known to drive a CO outflow (Bontemps et al. 1996; Sekimoto et al. 1997), with velocities as high as $\sim 80 \text{ km s}^{-1}$ (Boogert et al. 2002), although its morphology is unknown at the scales of the images presented here. In some Class I protostellar envelopes, both spatially diffuse H₂ emission and compact H₂ emission knots have been identified in the same source (Yamashita & Tamura 1992; Davis et al. 2002). In such cases, the diffuse component is found to trace the infrared continuum reflection nebula, whereas knotty, compact emission traces the fast jets observed at optical or cm-continuum wavelengths. By analogy, the knotty H₂ emission features identified in Figure 3b are likely to be associated with the jets driven by Elias 29. Since the cooling time of shocked 2.12 μm H₂ emission is on the order of a few years, the newly identified features in Figure 3b are tracing recent shock activity. The three H₂ emission features in Figure 5b: 1, 2a, and 2b, describe an S-shaped, point-symmetry, about the center, consistent with a precessing jet (Cliffe et al. 1995).

5.1 Comparison to hydrodynamic simulations

Recently, hydrodynamic simulations of precessing jets which create synthetic H_2 1–0 S(1) emission line images have become available (Rosen & Smith 2004; Smith & Rosen 2005). In the Smith & Rosen (2005) hydrodynamic simulations with fast jet precession, where the precession period is much less than the flow expansion time, the flow region has an axial cross-sectional shape of an annulus around a central region of trapped ambient gas. The molecular hydrogen 1-0 S(1) emission is primarily restricted to a ring near the leading shocks. As the flow evolves the ring fragments into multiple small bow shocks and has a chaotic structure (fig 6a & 6b). In simulations of slow precession, where the precession period is a large fraction of the expansion time, the cavities have lower density. In the case of the constant velocity slowly precessing jet, the H_2 shock emission has the appearance of a sinuous ribbon (figures 6c & 6d). The pulsed slowly precessing jet simulation shows an ordered chain of oblique bow shocks (figures 6e & 6f)

Comparison of the H_2 emission from Elias 29 with the synthetic H_2 1-0 S(1) model images leads to the conclusion that this jet exhibits slow, rather than fast, precession (fig 7). The discontinuities of the H_2 emission from Elias 29 are indicative of a pulsed jet, however the effects of variable extinction due

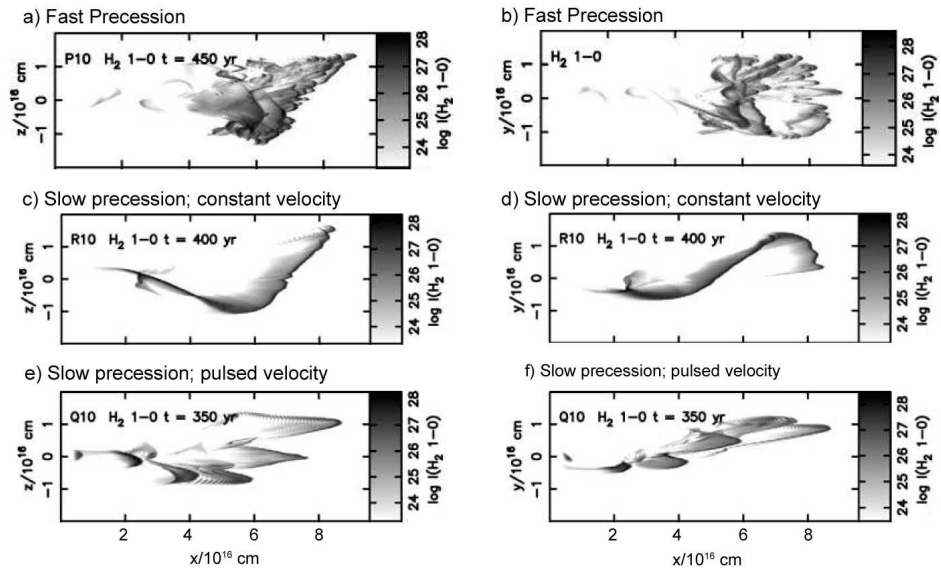


Figure 6: Synthetic H₂ 1-0 S(1) emission line images from the hydrodynamic simulations of Smith & Rosen (2005) (*Reprinted with permission of author*). The flow is in the x direction. For the z -axis and y -axis the units are 10^{16} cm. The separation between tick marks along the x -axis is 2×10^{16} cm. The luminosities are in erg s^{-1} .

to foreground clouds cannot be ruled out. The slow-precession models used a precession angle of 10° , however the precession angle of the Elias 29 jet may be wider based on the projected half-angle formed by Features 1 and 2a with the central symmetry axis of the observed reflection nebulosity.

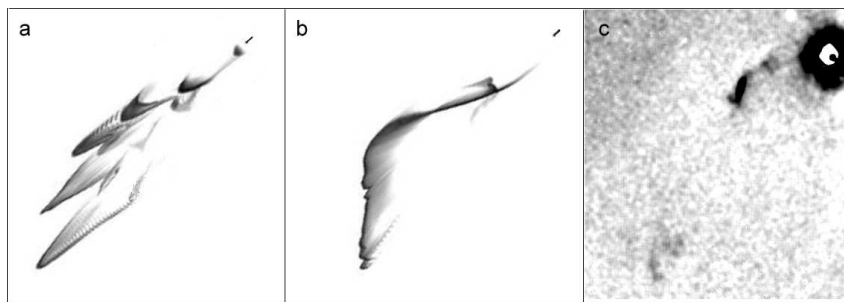


Figure 7: (a) Synthetic H₂ emission of pulsed slow-precessing jet simulation. (b) Synthetic H₂ emission of constant velocity slow-precessing jet simulation. (c) Observed H₂ emission from Elias 29.

5.2 Comparison to observations of other Young Stellar Objects

Images of both scattered light cavities and H₂ jet emission within them exist for only a handful of Class I objects (Davis et al. 2002). For all of these, the jets lie well within the outflow cavity walls, close to, if not precisely along, the symmetry axis of each outflow cavity. By contrast, the jet of Elias 29, as traced by H₂, is found close to, and, in one case (feature 2b) along, the cavity walls (Fig. 5b).

Examples of other *S*-shaped, precessing outflows are known (Gueth et al. 1996; Schwartz & Greene 1999; Hodapp et al. 2005; Sahai et al. 2005). However, no precessing protostellar jets have been imaged at their base within their scattered light cavities, either because they are too embedded to be detected in the NIR (L1157, HH211-mm), or because of lack of narrowband continuum data excluding the H₂ emission line for proper image subtraction (IRAS 03256+3055).

5.3 Precession Mechanisms

Binarity has inevitably been invoked to account for the presence of precessing jets (Terquem et al. 1999). However, Elias 29 is known to be single (Simon et al. 1995; Ghez et al. 1993). At scales between $\sim 1 - 60$ AU, lunar occultation observations show that 90% of the K-band flux from Elias 29 originates in a component ~ 7 mas diameter (~ 0.8 AU) with the remaining 10% of the K-band flux originating in a much larger, 415 mas diameter, diffuse component (Simon et al. 1987). It is then inferred that within ≈ 0.8 AU, Elias 29 is a single object. Alternative scenarios leading to jet precession that may be operative in Elias 29 might be disk oscillations associated with a propeller-driven outflow, recently discovered in MHD simulations (Romanova et al. 2006)

or warping of the accretion disk caused by the magnetically driven jets (Lai 2003). For the model of a warping accretion disk, a large-scale magnetic field threads through the disk. The disk's rotation twists the poloidal magnetic field creating a toroidal magnetic field that is discontinuous across the disk plane and induces a surface current on the disk. The interaction between the surface current and the external magnetic field provides a magnetic braking torque. If there is a perturbation in the disk so that a circular ring section is tilted while the rest of the disk is flat, there arises an additional torque on the disk that increases the tilt angle and thus creates the warping instability. Another torque arises from the perturbation which causes the perturbed ring to precess in a direction opposite to the disk rotation. Future high-resolution integral field spectroscopic observations of both the jet and the disk components could test this latter model.

5.4 Conclusion

High sensitivity narrowband images of the Class I protostar, Elias 29, unveil a precessing jet within the boundaries of the protostellar envelope. The H_2 emission features reveal recent shock activity along the wide-angle cavity walls indicating that the precessing jet is carving out the cavity. From comparing

the continuum subtracted H₂ images with the hydrodynamic models we infer that the jet exhibits slow precession.

References

- Arce, H. G. & Sargent, A.I. 2005, *ApJ*, 624, 232
- Allen, D.A. & Burton, M.G. 1993, *Nature*, 363, 54
- Barsony, M., Ward-Thompson, D., André, Ph., & O'Linger, J. 1998, *ApJ*, 509, 733
- Bence, S., Richer, J.S., & Padman, R. 1996, *MNRAS*, 279, 886
- Bontemps, S., André, P., Terebey, S., & Cabrit, S. 1996, *A&A*, 311, 858
- Boogert, A. C. A., Hogerheijde, M. R., Ceccarelli, C., Tielens, A. G. G. M., Van Dishoeck, E. F., Blake, G. A., Latter, W. B., & Motte, F. 2002, *ApJ*, 570, 708
- Cliffe, J. A., Frank, A., Livio, M., & Jones, T. W. 1995, *ApJL*, 447, L49
- Davis, C.J., Stern, L., Ray, T.P., & Chrysostomou, A. 2002, *A&A*, 382, 1021
- Eisloffel, J., Mundt, R., Ray, T.P., & Rodriguez, L. P. 2000, in *Protostars and Planets IV*, ed. Mannings, V., Boss, A. P., & Russell, S. S. (Tucson: The University of Arizona Press), 815
- Fridlund, C.V.M., Liseau, R., Djupvik, A.A., Hultgren, M., White, G.J., Favata, F. & Giardino, G. 2005, *A&A*, 436, 983
- Ghez, A., Neugebauer, G., & Matthews, K. 1993, *AJ*, 106, 2005
- Gómez, M., Stark, D. P., Whitney, B. A., & Churchwell, E. 2003, *AJ*, 126, 863
- Greene, T. P., & Lada, C. J. 1996, *AJ*, 112, 2184
- Gueth, F., Guilloteau, S., & Bachiller, R. 1996, *A&A*, 307, 891
- Hartigan, P., Morse, J., & Raymond, J. 1994, *ApJ*, 436, 125
- Hodapp, K. W. 1999, *AJ*, 118, 1338
- Hodapp, K.W., Bally, J., Eisloffel, J., & Davis, C.J. 2005, *AJ*, 129, 1580
- Hollenbach, D. J., & Shull, J. M. 1977, *ApJ*, 216, 419
- Khazadyan, T., Gredel, R., Smith, M. D., & Stanke, T. 2004, *A&A*, 426, 171

- Königl, A. & Pudritz, R. E. 2000, in *Protostars and Planets IV*, ed. Mannings, V., Boss, A. P., & Russell, S. S. (Tucson: The University of Arizona Press), 759
- Lai, D. 2003, *ApJL*, 591, L119
- Lepp, S. & Shull, J. M. 1983, *ApJ*, 270, 578
- Lim, A.J. 2001, *MNRAS*, 327, 507
- Liseau, R., Fridlund, C.V.M., & Larsson, B. 2005, *ApJ*, 619, 959
- Martini, P., Persson, S.E., Murphy, D.C., Birk, C., Shectman, S.A., Gunnels, S.M., Koch, E. 2004, *Proc. SPIE*, 5492, 1653
- Masson, C.R. & Chernin, L. 1993, *ApJ*, 414, 230
- Mundt, R. & Fried, J.W. 1983, *ApJ*, 274, 83
- Mundt, R., Bührke, T., Solf, J., Ray, T.P., & Raga, A.C. 1990, *A&A*, 232, 37
- Parker, N.D., Padman, R., & Scott, P.F. 1991, *MNRAS*, 252, 442
- Reipurth, B., Bally, J., & Devine, D. 1997, *AJ*, 114, 2708
- Romanova, M.M., Ustyugova, G.V., Koldoba, A.V., & R.V.E. Lovelace 2006, *ApJL*, 635, L165
- Reipurth, B. & Bally, J. 2001, *ARAA*, 39, 403
- Shull, J. M., & Hollenbach, D. J. 1978, *ApJ*, 220, 525
- Richer, J. S., Shepherd, D. S., Cabrit, S., & Churchwell, E. 2000, in *Protostars and Planets IV*, ed. Mannings, V., Boss, A. P., & Russell, S.
- Shull, J. M., & Hollenbach, D. J. 1978, *ApJ*, 220, 525 S. (Tucson: The University of Arizona Press), 867
- Rosen, A., & Smith, M. D. 2004, *MNRAS*, 347, 1097
- Sahai, R., Le Mignant, D., Sánchez Contreras, C., Campbell, R. D., & Chaffee, F. H. 2005, *ApJL*, 622, L53
- Sandell, G. & 18 co-authors 1999, *ApJ*, 519, 236

- Schwartz, R.D. & Greene, T. P. 1999, *AJ*, 117, 456
- Sekimoto, Y., Tatematsu, K., Umemoto, T., Koyama, K., Tsuboi, Y., Hirano, N., & Yamamoto, S. 1991, *ApJL*, 489, L63
- Shu, F. H., Najita, J., Ostriker, E. C., & Shang, H. 1995, *ApJL*, 455, L155
- Shull, J.M. & Beckwith, S., *ARAA*, 20, 163
- Snell, R.L., Loren, R.B., & Plambeck, R.L. 1980, *ApJL*, 239, L17
- Simon, M., Howell, R.R., Longmore, A.J., Wilking, B.A., Peterson, D.M., & Chen, W.P. 1987, *ApJ*, 320, 344
- Simon, M., Ghez, A.M., Leinert, Ch., Cassar, L., Chen, W.P., Howell, R.R., Jameson, R.F.m Matthews, K., Neugebauer, G., & Richichi, A. 1995, *ApJ*, 443, 625
- Smith M. D. & Rosen, A. 2005, *MNRAS*, 357, 579
- Snell, R.L., Bally, J., Strom, S.E., & Strom, K.M. 1985, *ApJ*, 290, 587
- Stoche, J., Hartigan, P.M., Strom, S.E., Strom, K.M., Anderson, E.R., Hartmann, L, & Kenyon, S.J. 1988, *ApJS*, 68, 229
- Skrutskie, M. F., Cutri, R.M., Stiening, R., Weinberg, M.D., Schneider, S., Carpenter, J.M., Beichman, C., Capps, R., Chester, T., Elias, J., Huchra, J., Liebert, J., Lonsdale, C., Monet, D.G., Price, S., Seitzer, P., Jarrett, T., Kirkpatrick, J.D., Gizis, J., Howard, E., Evans, T., Fowler, J., Fullmer, L., Hurt, R., Light, R., Kopan, E.L., Marsh, K.A., McCallon, H.L., Tam, R., Van Dyk, S., and S. Wheelock, 2006, *AJ*, 131, 1163
- Terquem, C., Eislöffel, J., Papaloizou, J., & Nelson, R.P. 1999, *ApJL*, 512, L131
- Whitney, B.A., Wood, K., Bjorkman, J.E., & Cohen, M. 2003, *ApJ*, 598, 1079
- Wilson, J.E., Eikenberry, S.S., Henderson, C.P., Hayward, T.L., Carson, J.C., Pirger, B., Barry, D.J., Brandl, B.R., Houck, J.R., Fitzgerald, G., & Stolberg, T.M. 2003, *Proc. SPIE*, 4841, 451
- Wolf-Chase, G.A., Barsony, M., & O'Linger, J. 2000, *AJ*, 120, 1467

Yamashita, T. & Tamura, M. 1992, ApJL, 387, L93

Yun, J.C., Santos, C.A., Clemens, D.P., Afonso, J.M., McCaughrean, M.J.,
Preibisch, T., Stanke, T., & H. Zinnecker 2001, A&A, 372, L33

Zuckerman, B., Kuiper, T.B.H., Rodriguez-Kuiper, E.N. 1976, ApJL, 209,
L137

A IRAF grid.cl script

```
# CL to reduce grid data taken in a long sequence
# from grid.cl by Karl Haisch, 2/10/99
# Modified by Jason Ybarra, 6/2005

procedure grid (inimage, pref)

string inimage {prompt="List of input images"}
string pref    {prompt="Prefix to attach to flattened images"}
struct *inlist

begin
string im, timage, m1, m2, m3, m4, p1, p2, p3, p4
string comlist, tpref
int i

comlist=inimage
inlist=comlist
tpref=pref
#
# start by doing the first five images
#

i = fscan (inlist ,m4)
i = fscan (inlist ,m3)
i = fscan (inlist ,m2)
i = fscan (inlist ,m1)
i = fscan (inlist ,im)
i = fscan (inlist ,p1)
i = fscan (inlist ,p2)
i = fscan (inlist ,p3)
i = fscan (inlist ,p4)

# make a sky background image

comlist="s"//im//",s"//m4//",s"//m3//",s"//m2//",s"//m1
```

```

comlist=comlist//",s"//p1//",s"//p2//",s"//p3//",s"//p4
imdel ('tflat')
imcomb(comlist, 'tflat', combine="med", reject="avsigclip",
        scale="med", lsigma=2.5, hsigma=2.5, zero-)

# subtract the sky

imarith(m4, '-', 'tflat', tpref//m4)
imarith(m3, '-', 'tflat', tpref//m3)
imarith(m2, '-', 'tflat', tpref//m2)
imarith(m1, '-', 'tflat', tpref//m1)
imarith(im, '-', 'tflat', tpref//im)

# this is the main loop to do all but the last three

while(fscan(inlist, timage) !=EOF) {

m4=m3
m3=m2
m2=m1
m1=im
im=p1
p1=p2
p2=p3
p3=p4
p4=timage

# make the flat

comlist="s"//im//",s"//m4//",s"//m3//",s"//m2//",s"//m1
comlist=comlist//",s"//p1//",s"//p2//",s"//p3//",s"//p4
imdel ('tflat')
imcomb(comlist, 'tflat', combine="med", reject="avsigclip",
        scale="med", lsigma=2.5, hsigma=2.5, zero-)

# subtract the sky

```

```
    imarith(im, '-', 'tflat', tpref//im)

}

# do the last 4

# make the flat

imdel('tflat')
comlist=comlist//",s"//im
imcomb(comlist, 'tflat', combine="med", reject="avsigclip",
       scale="med",lsigma=2.5, hsigma=2.5, zero-)

# sky subtract

imarith(p4, '-', 'tflat', tpref//p4)
imarith(p3, '-', 'tflat', tpref//p3)
imarith(p2, '-', 'tflat', tpref//p2)
imarith(p1, '-', 'tflat', tpref//p1)

end
```